

# Natural Image Stitching Using Depth Maps

Tianli Liao

Henan University of Technology  
Zhengzhou 450001, China

tianli.liao@haut.edu.cn

Nan Li

Shenzhen University  
Shenzhen 518060, China

nan.li@szu.edu.cn

## Abstract

*Natural image stitching (NIS) aims to create one natural-looking mosaic from two overlapping images that capture a same 3D scene from different viewing positions. Challenges inevitably arise when the scene is non-planar and the camera baseline is wide, since parallax becomes not negligible in such cases. In this paper, we propose a novel NIS method using depth maps, which generates natural-looking mosaics against parallax in both overlapping and non-overlapping regions. Firstly, we estimate a pixel-to-pixel transformation based on feature matches and their depth values. Then, we draw a triangulation of the target image and estimate multiple local homographies, one per triangle, based on the locations of their vertices and the rectified depth values. Finally, the warping image is composited by the backward mapping of piece-wise homographies. Experimental results demonstrate that the proposed method not only provides accurate alignment in the overlapping regions, but also virtual naturalness in the non-overlapping region.*

## 1. Introduction

Natural image stitching (NIS) is a well-studied problem in computer vision, which composites multiple overlapping images captured from different viewing positions into one natural-looking panorama [25]. The fundamental NIS problem is 2-into-1: given two input images, one reference and one target, to generate one output image that is virtually captured in the reference viewing position, which includes both overlapping and non-overlapping contents as natural as possible. Hence, the first crucial task in NIS is how to warp the target image into an extended view of the reference image, such that the warping result is not only *content-consistent* in the overlapping region but also *view-consistent* in the non-overlapping region.

When the capturing scene is planar or the viewing point is stationary, homography is effective for accomplishing the dual task [9]. However, when the 3D scene consists of background objects with non-planar surfaces or even foreground

objects with discontinuous depths, meanwhile the baseline is wide, homography cannot generate a natural-looking mosaic because it is not flexible enough to describe the underlying 3D geometry between parallax views (see Fig. 1(b)).

Lots of adaptive warping models are devoted to addressing the parallax issue in NIS. Suppose a set of feature matches between two input images are given, some methods divide the target image into adjacent patches (pixels [6], superpixels [13], rectangles [28], triangles [14], irregular domains [31]) and warp each of them by a local homography using weighted matches; some methods divide the target into rectangular cells and deform them simultaneously via an energy minimization using local (similar [29] or affine [30]) plus global (similar [4] or linearized projective [17]) geometric invariants. Other NIS methods devote attention to combining weighted matches and geometric invariants [2, 15, 18], increasing densities of feature matches [16, 20], pursuing local alignment allowing seamless composition [7, 19]. Nevertheless, existing adaptive warping models are still not fine enough to describe the underlying geometry between large-parallax views such that they still create misaligned or non-natural-looking mosaics at times (see Fig. 1(c-e)).

It is well-known that depth maps are powerful for representing the 3D geometry of a stereo scene and deep learning enables extracting the dense depth map from a single target image [8]. Intuitively, depth maps help align non-matching region or even non-overlapping region (see Fig. 1(f)).

In this paper, we propose a new NIS method using depth maps against large parallax in both the overlapping and non-overlapping regions. Suppose a set of feature point matches between input images and a depth map of the target image are given, firstly we estimate a pixel-to-pixel transformation based on point matches and their depth values; then we draw a triangulation of the target image such that every triangle domain is coplanar in the 3D space; local homographies are estimated, one per triangle, based on locations of its vertices and their rectified depth values; finally the warping image is generated by backward mapping piece-wise homographies. Experimental results show that the stitching mosaics by the

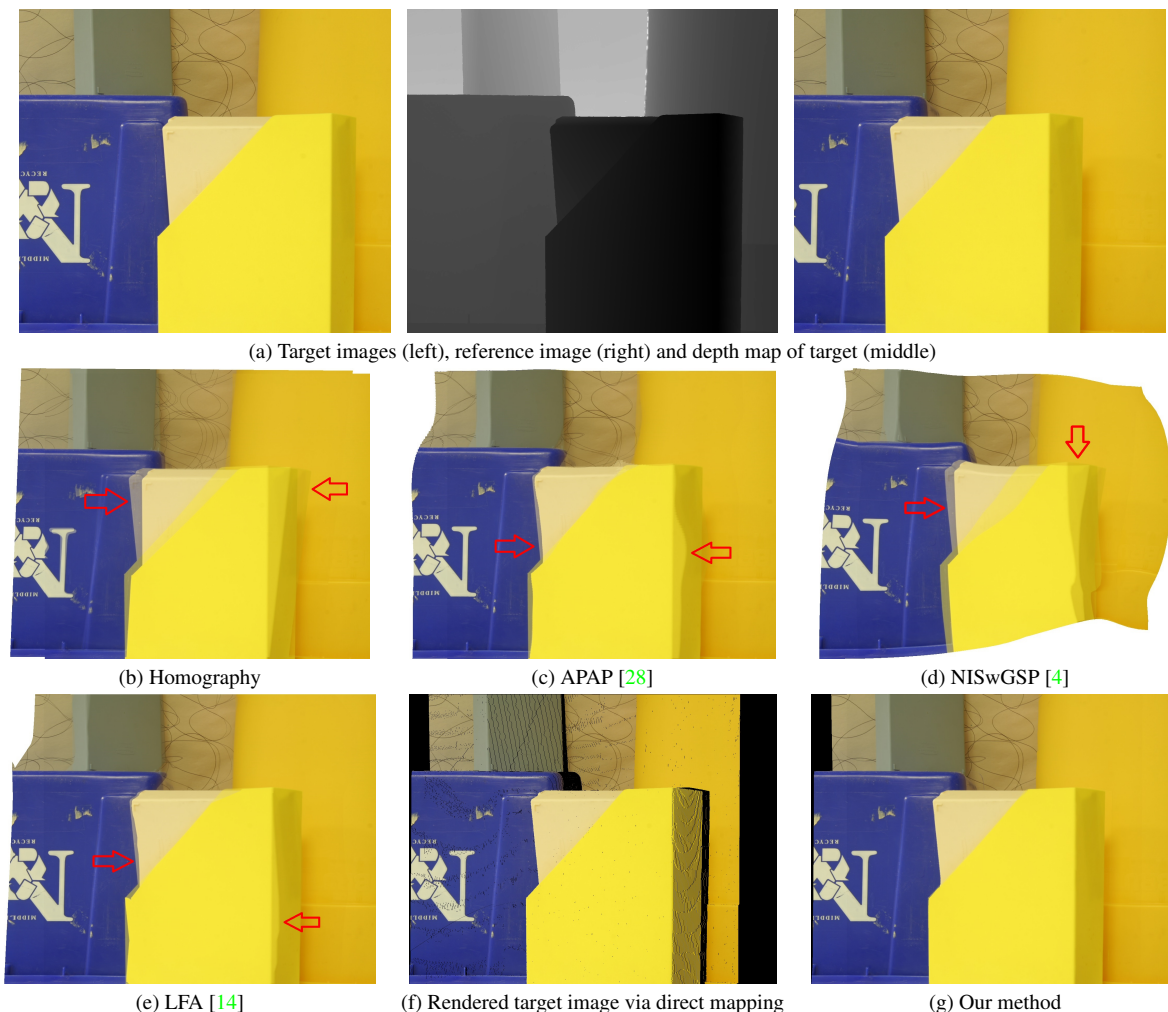


Figure 1. Stitching results of the *Plastic* test case from Middlebury [23] via various methods. All results are generated via simple average blending, except that (f) is the rendered target image via direct mapping (best view in color and zoom in).

proposed NIS method are not only accurately aligned in the overlapping regions but also virtually natural-looking in the non-overlapping regions (see Fig. 1(g)).

The rest of the paper is organized as follows. Section 2 reviews the related works of adaptive NIS and view synthesis. Section 3 proposes the novel NIS method using depth maps. Section 4 describes the implementation details. Section 5 presents the experimental results. Section 6 concludes the paper.

## 2. Related Work

**NIS using weighted matches** Suppose a set of feature matches between two input images is given, some NIS methods adopted piece-wise homographies as adaptive warping models where every local homography is determined via some weighting methods. Gao *et al.* proposed a dual-homography warping model, where two represen-

tative homographies (distant plane + ground plane) are first clustered then the local homography per pixel is estimated by a weighted sum of them [6]. Zheng *et al.* modified a multiple-homography warping model, where multiple projective-consistent homographies are first clustered and one non-overlapping homography is averaged, then the local homography per pixel is determined by a weighted sum of them [31]. Zaragoza *et al.* proposed a new as-projective-as-possible (APAP) warp, where the target image is first divided into regular grid cells and the local homography per cell is estimated by moving DLT that assigns more weights to feature matches that located closer to the target cell [28]. Joo *et al.* appended line matches into the framework of APAP [12]. Recently, Lee and Sim proposed a modified version of APAP, where the target image is divided into superpixels instead of cells and the local homography per superpixel is estimated by moving DLT which assigns more

weights to feature points that located on more similar planar regions to the target superpixel instead of explicitly depending on the spatial locations [13]. The most notable advantage of [13] is that it enables a discontinuous warping model against large parallax in the overlapping region. Besides, Li *et al.* proposed a weighting-free version of APAP, where the target image is divided into adjacent triangle regions whose vertices are either matching feature points or boundary points, then the local homography per triangle is estimated by its vertex matches associated with the relative position between two input views [14]. The advantage of triangulation is apparent as triangles are easier to fulfill coplanar assumption than other patches. However, [14] did not allow vertex split such that large parallax can not be handled. On the contrary, the proposed method uses depth maps to enable triangulation vertex split to handle large parallax not only in the overlapping but also in the non-overlapping regions.

**NIS using geometric invariants** Instead of using weighted matches to warping non-matching patches, some NIS methods divide the target image into cells then warp them simultaneously by a deformation, where every mesh is penalized to undergo some geometric invariants (local + global) as much as possible. Zhang and Liu proposed a mesh deformation that uses similar as local geometric invariant and projective as global geometric invariant [29]. Chen and Chuang used similar as both local and global geometric invariants [4]. The estimations of global similarity were comprehensively studied in [2, 18]. In order to address the NIS problem for wide-baseline images, Zhang *et al.* proposed a mesh deformation that uses affine as local geometric invariant and horizontal-perpendicular-preserving as global geometric invariant [30]. In order to generate perspective-consistent mosaics, Liao and Li used linearized projective [15] as both local and global geometric invariants [17]. Recently, Jia *et al.* proposed a new local coplanar invariant and a new global collinear invariant [11]. Note that local and global geometric invariants play the roles of interpolation and extrapolation regularizers in the overlapping and non-overlapping regions respectively, while the depth map of the target image can provide more accurate regularizers.

**View synthesis using depth maps** Generally speaking, view synthesis (view interpolation) [3] is the task of generating new views of a 3D scene from source views of the scene, where depth maps are commonly adopted to describe the 3D scene from source viewing positions. There are different methods to extract depth maps of source images. Penner and Zhang used depth estimation from multiple images to accomplish novel view synthesis [22]. Wiles *et al.* leveraged single-image depth predictions implicitly to enable end-to-end view synthesis [27]. In fact, image warping in NIS can also be interpreted as extended view synthesis, taking the target image as the source image and the refer-

ence view as the virtual view. However, this paper focuses on using depth maps to improve both alignment and naturalness for NIS rather than appearance modeling [32] and occlusion inpainting in view synthesis tasks [24].

### 3. Proposed Method

In this section, we propose our NIS method using depth maps.

**Notations:** let the upper-case letters such as  $K, R, H$  denote real matrices, the lower-case letters such as  $x, y, z$  denote real values, the bold-faced letters such as  $\mathbf{x}, \mathbf{e}'$  denote real vectors; the symbol  $\tilde{\mathbf{x}}$  denotes the homogeneous representation of  $\mathbf{x}$ , the symbol  $[\mathbf{e}']_{\times}$  denotes the skew-symmetric matrix formulated by  $\mathbf{e}'$ .

#### 3.1. P2P transformation using depth maps

Given a target image  $I_t$  and a reference image  $I_r$ , suppose their camera matrices are:

$$P = K[I | \mathbf{0}], \quad P' = K'[R | \mathbf{t}], \quad (1)$$

where  $K \in \mathbb{R}^{3 \times 3}$  and  $K' \in \mathbb{R}^{3 \times 3}$  are two calibration matrices,  $R \in \text{SO}(3)$  is a rotation and  $\mathbf{t} \in \mathbb{R}^3$  is a translation.

Let  $\mathbf{X} \in \mathbb{R}^3$  be a world point,  $\mathbf{x} \in \mathbb{R}^2$  and  $\mathbf{x}' \in \mathbb{R}^2$  be its image points in  $I_t$  and  $I_r$ , and  $z \in \mathbb{R}$  be its depth value measured from  $P$ , then

$$\tilde{\mathbf{x}} = K\mathbf{X}/z. \quad (2)$$

Since  $K$  is invertible, by plugging  $\mathbf{X} = zK^{-1}\tilde{\mathbf{x}}$  into

$$\tilde{\mathbf{x}}' \sim K'R\mathbf{X} + K'\mathbf{t}, \quad (3)$$

where  $\sim$  denotes equality up to scale, we obtain

$$\tilde{\mathbf{x}}' \sim K'RK^{-1}\tilde{\mathbf{x}} + K'\mathbf{t}/z. \quad (4)$$

Let  $H_{\infty} = K'RK^{-1}$  and  $\mathbf{e}' = K'\mathbf{t}$ , we simplify (4) as

$$\tilde{\mathbf{x}}' \sim H_{\infty}\tilde{\mathbf{x}} + \mathbf{e}'/z. \quad (5)$$

In fact,  $H_{\infty}$  is the infinite homography between two parallax views and  $\mathbf{e}'$  is the epipole in the view of  $I_r$ .

Suppose a set of feature point matches between  $I_t$  and  $I_r$ , and their corresponding depth values from  $P$  are given, then one can estimate  $H_{\infty}$  and  $\mathbf{e}'$  based on (5). Conversely, when  $H_{\infty}$  and  $\mathbf{e}'$  are known, a pixel-to-pixel (P2P) transformation from  $I_t$  to  $I_r$  can be established via (5) if a dense depth map of  $I_t$  is given. The implementation details about estimating  $H_{\infty}$  and  $\mathbf{e}'$  will be presented in Sec. 4.1.

With the P2P transformation, one can directly render the warped target image via forward mapping. Fig. 1(f) shows the direct mapping result from Fig. 1(a), where the ‘‘continuous’’ black regions indicate the existing parallax between

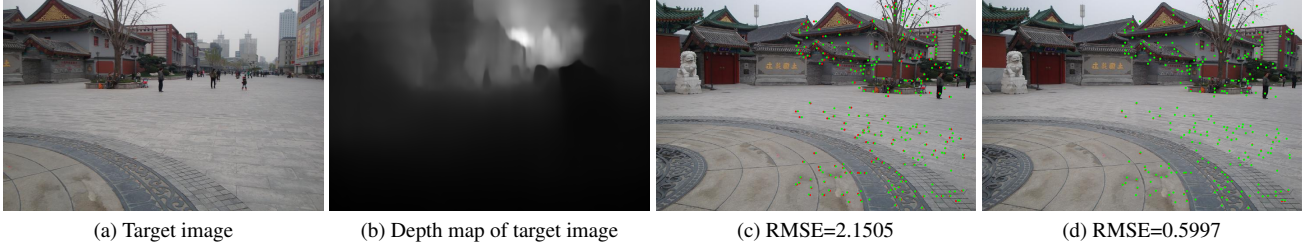


Figure 2. Alignment errors via direct mapping. (a) is target image of *temple* test case in [6]. (b) is depth map of (a) via monodepth2 [8]. (c) and (d) are the alignment errors via direct mapping and our local warping model respectively. **Red** indicates SIFT points in reference and **green** indicates the warped SIFT points from target. The RMSE is calculated via  $\sqrt{\frac{1}{m} \sum_{i=1}^m (\mathbf{q}_i - \omega(\mathbf{p}_i))^2}$ , where  $\omega: I_t \rightarrow I_r$ .

two views and the “discrete” black spots indicate the missing pixels due to forward mapping.

Another thing should be noted is that the P2P transformation may suffer alignment errors when the depth map is not reliable enough. Fig. 2 show the alignment errors of SIFT point matches via direct mapping. Thus, in order to improve the alignment accuracy and enable the backward mapping, a local warping method using depth maps is proposed subsequently.

### 3.2. Local homography using depth maps

Let us consider the 3-parameter family of world planes across  $\mathbf{X}$ ,

$$\mathbf{m}^T \mathbf{K} \mathbf{X} = 1, \quad (6)$$

where  $\mathbf{m} \in \mathbb{R}^3$ . Consequently, by multiplying the row vector  $\mathbf{m}^T$  to (2), we obtain

$$\mathbf{m}^T \tilde{\mathbf{x}} = 1/z, \quad (7)$$

which means that a plane can be uniquely determined from three non-collinear image points and their depth values.

Furthermore, by plugging (7) into (5), we derive

$$\tilde{\mathbf{x}}' \sim \mathbf{H}_\infty \tilde{\mathbf{x}} + \mathbf{e}' \mathbf{m}^T \tilde{\mathbf{x}}. \quad (8)$$

It is well known that the images of a world plane between two views satisfy a homography. Therefore,

$$\mathbf{H} = \mathbf{H}_\infty + \mathbf{e}' \mathbf{m}^T, \quad (9)$$

describes the 3-parameter family of homographies between two different views induced by a world plane (6).

Given a triangular domain  $\Delta$  of  $I_t$  and three depth values of its vertices measured from P, assuming that its corresponding world point set is coplanar, then we can determine  $\mathbf{m}_\Delta$  based on (7). Conversely, when a triangulation of  $I_t$  is given such that every  $\Delta$  is coplanar in the 3D space, then the local homography  $\mathbf{H}_\Delta$ , one per triangle, can be established by (9) with estimated  $\mathbf{m}_\Delta$ .

The implementation details about estimating  $\mathbf{m}_\Delta$  will be presented in Sec. 4.2.

### 3.3. Image warping via piece-wise homographies

Finally, the warping image  $I_w$  is generated by the backward mapping of piece-wise homographies:

$$I_w(\mathbf{x}') = I_t \left( \pi \left( \mathbf{H}_\Delta^{-1}(\tilde{\mathbf{x}}') \right) \right), \quad \forall \mathbf{x}' \in \Delta', \quad (10)$$

where  $\Delta'$  is the triangular domain of  $\Delta$  which is forward mapped by  $\mathbf{H}_\Delta$  and  $\pi(\mathbf{v}) = (v_1/v_3, v_2/v_3)^T$  for  $\mathbf{v} \in \mathbb{R}^3$ .

Note that two adjacent domains in  $I_t$  may become overlapping in  $I_w$  after mapping by different homographies. The implementation details about backward texture mapping by  $\{\mathbf{H}_\Delta^{-1}\}$  will be presented in Sec. 4.3.

## 4. Implementation

In this section, we present some implementation details of the proposed method.

### 4.1. Estimating infinite homography and epipole

In order to estimate  $\mathbf{H}_\infty$  and  $\mathbf{e}'$ , we firstly prepare a set of SIFT [21] point matches  $\{(\mathbf{p}_i, \mathbf{q}_i)\}_{i=1}^N$  between  $I_t$  and  $I_r$ , a depth map  $z = d(\mathbf{x})$  of  $I_t$  which can be directly obtained from RGBD datasets or estimated via monodepth2 [8] if the depth data are unavailable.

Similar to the DLT algorithm for estimating homography from a data set  $\{(\mathbf{p}_i, \mathbf{q}_i)\}_{i=1}^N$ ,  $\mathbf{H}_\infty$  and  $\mathbf{e}'$  can be estimated from the augmented data set  $\{(\mathbf{p}_i, \mathbf{q}_i, d(\mathbf{p}_i))\}_{i=1}^N$  via solving the following linear least-square problem

$$\min_{\mathbf{h}, \mathbf{e}'} \|\mathbf{A} \mathbf{h} + \mathbf{B} \mathbf{e}'\|^2, \quad (11)$$

where  $\mathbf{h}$  is a 9-vector made up of the entries of  $\mathbf{H}_\infty$ , and the matrices  $\mathbf{A}$  and  $\mathbf{B}$  are vertically stacked by

$$\mathbf{A}_i = \begin{bmatrix} x_i & y_i & 1 & 0 & 0 & 0 & -x_i x'_i & -x'_i y_i & -x'_i \\ 0 & 0 & 0 & x_i & y_i & 1 & -x_i y'_i & -y_i y'_i & -y'_i \end{bmatrix}$$

$$\mathbf{B}_i = \begin{bmatrix} 1/z_i & 0 & -x'_i/z_i \\ 0 & 1/z_i & -y'_i/z_i \end{bmatrix}$$



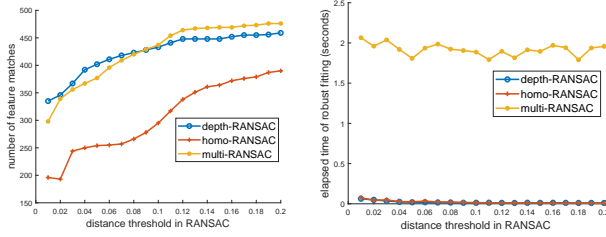


Figure 3. Comparison of robust fitting methods on number of feature matches and elapsed time of the *Plastic* test case.

for  $i = 1, \dots, N$ ,  $(x_i, y_i)$  and  $(x'_i, y'_i)$  are coordinates of  $\mathbf{p}_i$  and  $\mathbf{q}_i$ ,  $z_i = d(\mathbf{p}_i)$ . When  $N \geq 6$ , (11) can be efficiently solved by Singular Value Decomposition (SVD).

For the sake of more robust estimation, we employ the 6-point SVD solver as the minimal solver in the RANSAC framework. With the help of depth data, a single RANSAC estimator can identify a sufficiently large consensus set of point matches between parallax views, while existing methods need multiple RANSAC estimators to identify multiple homographies.

Fig. 3 shows a comparison result of feature matches via three robust fitting methods: homography-based RANSAC [5] (homo-RANSAC), multiple-sampling RANSAC [28] (multi-RANSAC) and the depth-based RANSAC (depth-RANSAC). The depth-RANSAC method can identify sufficiently many feature matches meanwhile take the least time (even less than homo-RANSAC sometimes).

For the sake of more accurate estimation,  $H_\infty$  and  $\mathbf{e}'$  are refined by solving the following nonlinear LS problem

$$\min_{H_\infty, \mathbf{e}'} \sum_{i \in \text{IS}} \|\pi(H_\infty \tilde{\mathbf{p}}_i + \mathbf{e}'/z_i) - \mathbf{q}_i\|^2 \quad (12)$$

where IS is the index set of identified inliers from the RANSAC estimator. (12) can be efficiently solved by the Levenberg-Marquardt (LM) algorithm.

The algorithm for estimating  $H_\infty$  and  $\mathbf{e}'$  is summarized in Algorithm 1.

---

**Algorithm 1** Estimate  $H_\infty$  and  $\mathbf{e}'$ .

---

**Require:**  $\{(\mathbf{p}_i, \mathbf{q}_i)\}_{i=1}^N$  and  $\{z_i = d(\mathbf{p}_i)\}$ ;

**Ensure:**  $\hat{H}_\infty$  and  $\hat{\mathbf{e}}'$ .

- 1: Initialize  $\hat{H}_\infty$ ,  $\hat{\mathbf{e}}'$  and IS via RANSAC with a minimal six-point SVD solver (11);
  - 2: Refine  $\hat{H}_\infty$  and  $\hat{\mathbf{e}}'$  by optimizing (12) with IS;
  - 3: Return  $\hat{H}_\infty$  and  $\hat{\mathbf{e}}'$ .
- 

## 4.2. Estimating local homographies

In order to establish multiple local homographies  $\{H_\Delta\}$ , we first partition the target image into SLIC [1] segments

based on its depth map and perform polygonal fitting on the border of each segment. Denote the vertex set by  $\{\mathbf{v}_j\}_{j=1}^M$  consisting of all point matches in the target image and all polygon vertices, then the triangulation can be calculated by the Delaunay triangulation algorithm (see Fig. 5).

For the sake of better local alignment, we first rectify the depth value of every matched point  $\mathbf{p}_i$  by

$$\frac{1}{z_i} = \frac{(\tilde{\mathbf{y}}' \times \mathbf{e}')^T (\tilde{\mathbf{y}}' \times H_\infty \tilde{\mathbf{y}})}{\|\tilde{\mathbf{y}}' \times \mathbf{e}'\|^2} \quad (13)$$

where  $(\tilde{\mathbf{y}}, \tilde{\mathbf{y}}')$  is the corrected point match that minimizes the reprojection error subject to the epipolar constraint, i.e., the optimal solution of

$$\begin{aligned} \min_{\mathbf{x}, \mathbf{x}'} \quad & \|\mathbf{p}_i - \mathbf{x}\|^2 + \|\mathbf{q}_i - \mathbf{x}'\|^2 \\ \text{subject to} \quad & \tilde{\mathbf{x}}'^T [\mathbf{e}']_\times H_\infty \tilde{\mathbf{x}} = 0. \end{aligned}$$

After the above depth rectification, the equation (7) will enable an optimal three-parameter family of homography for accurate local alignment at the vertex.

For the sake of better local naturalness, we then rectify the depth value of every vertex  $\mathbf{v}_j$ , triangle-by-triangle by

$$\frac{1}{z_{j,\Delta}} = \tilde{\mathbf{m}}_\Delta^T \tilde{\mathbf{v}}_j \quad (14)$$

where  $\tilde{\mathbf{m}}_\Delta$  is the parameter that best fits the inner points inside the triangle into a plane, i.e., the optimal solution of

$$\min_{\mathbf{m}_\Delta} \|C_\Delta \mathbf{m}_\Delta - \mathbf{d}_\Delta\|^2$$

where  $C_\Delta$  and  $\mathbf{d}_\Delta$  are stacked vertically by

$$C_k = \begin{bmatrix} x_k & y_k & 1 \end{bmatrix}, d_k = 1/z_k, \forall (x_k, y_k) \in \text{int}(\Delta).$$

After the above depth rectification, the equation (7) will enable an optimal 3-parameter family of homography for planar local naturalness inside the triangle.

In order to enable a globally discontinuous and locally smooth warping model, the multiple rectified depth values of the same vertex should be further clustered and averaged.

Global discontinuity means that one vertex  $\mathbf{v}_j$  should be allowed to split into some disjointed vertices after warping. For multiple depth values of a vertex, if the maximal difference is less than a threshold  $\eta$ , we consider them to be of the same class, otherwise we cluster them into different classes via a multiple-model fitting method [10], i.e.,

$$\min_{\mathbf{L}} E(\mathbf{L}) = \sum_p \|p - L_p\| + \beta \cdot |\mathcal{L}_L|. \quad (15)$$

Fig. 5 shows the experimental results of vertices clustering.

Local smoothness means that those triangles sharing a common vertex after warping should share the same depth

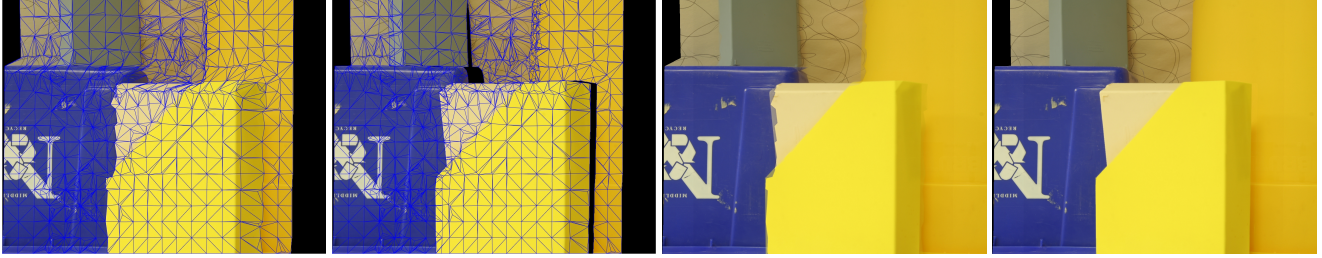


Figure 4. Ablation study on depth rectification. From left to right: Warped triangles w/o or w/ depth rectification. Panorama results w/o or w/ depth rectification (best view in color and zoom-in).

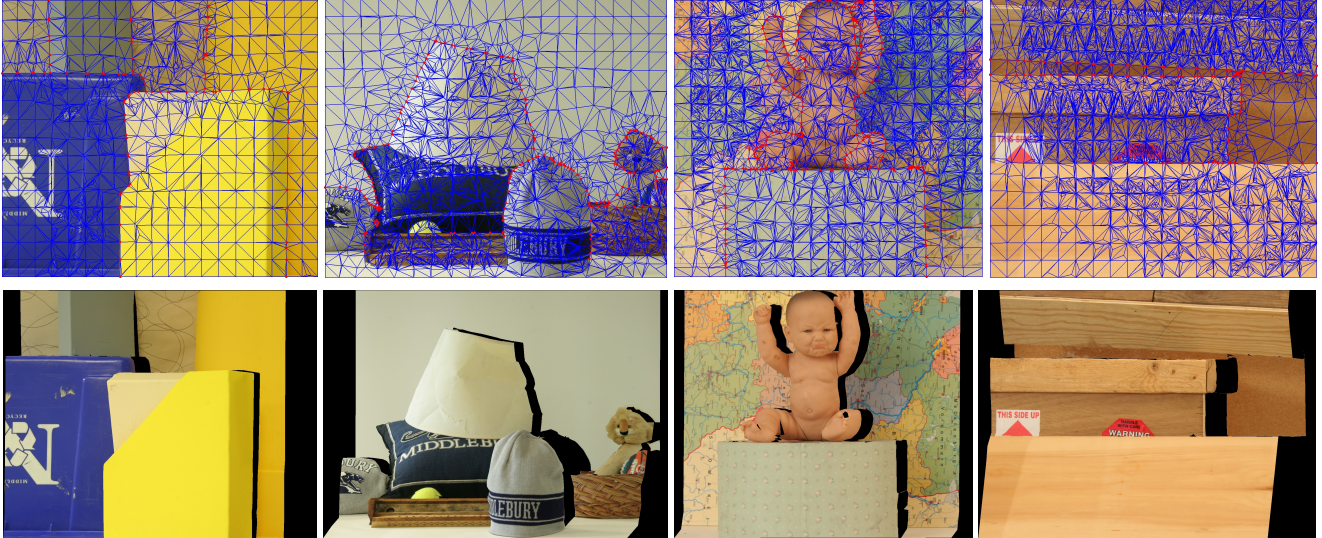


Figure 5. Results of Delaunay triangulation, vertices clustering and backward texture mapping on Middlebury datasets. Test cases from left to right are (*Plastic*, *Midd2*, *Baby1*, *Wood2*), respectively. Red dots in the first row represent the splitting vertices. Black regions in the second row indicate the parallax between input images.

value at this common vertex before warping. Therefore, we assign the average of multiple depth values inside their member class to the common vertex. Note that, for the class that includes the rectified depth value of a matched feature point, we assign that value rather than the average to the common vertex.

Fig. 4 shows an ablation study about local homographies estimation. Without depth rectification on triangle vertices, parallax regions are hardly to be aligned, which results in misalignments in the stitching result.

The algorithm for estimating  $\{H_{\Delta}\}$  for triangles is summarized in Algorithm 2.

### 4.3. Backward texture mapping

Since vertices splitting is allowed, the splitting triangles may be overlapping with each other in the overlapping region and even the non-overlapping region. When such case happens, i.e. two different local homographies  $H_{\Delta}$  and  $H_{\Delta'}$  map two different point  $\mathbf{p}$  and  $\mathbf{p}'$  in  $I_t$  to the same point  $\mathbf{q}$

---

#### Algorithm 2 Estimate $\{H_{\Delta}\}$ .

---

**Require:**  $\{\Delta\}$ ,  $\{(\mathbf{p}_i, \mathbf{q}_i)\}_{i \in IS}$  and  $d(I)$ ;

**Ensure:**  $\{H_{\Delta}\}$ .

- 1: For every  $\mathbf{p}_i$ , rectify its depth value by (13);
  - 2: For every  $\Delta$ , rectify the depth value of  $\mathbf{v}_j$  by (14);
  - 3: For every  $\mathbf{v}_j$ , cluster its multiple depth values;
  - 4: For every  $\Delta$ , finalize the depth value of  $\mathbf{v}_j$  as the average of its member class then solve (7) to get  $\mathbf{m}_{\Delta}$ ;
  - 5: Return  $\{H_{\Delta}\}$  that formulated by (9) with  $\{\mathbf{m}_{\Delta}\}$ .
- 

in  $I_w$ , we compare  $d(H_{\Delta}^{-1}(\hat{\mathbf{q}}))$  with  $d(H_{\Delta'}^{-1}(\hat{\mathbf{q}}))$  and use the pixel with the smaller depth value in the backward texture mapping, because it is closer to camera.

Fig. 5 shows some experimental results of backward texture mapping.

Finally, we summarize our method in Algorithm 3.



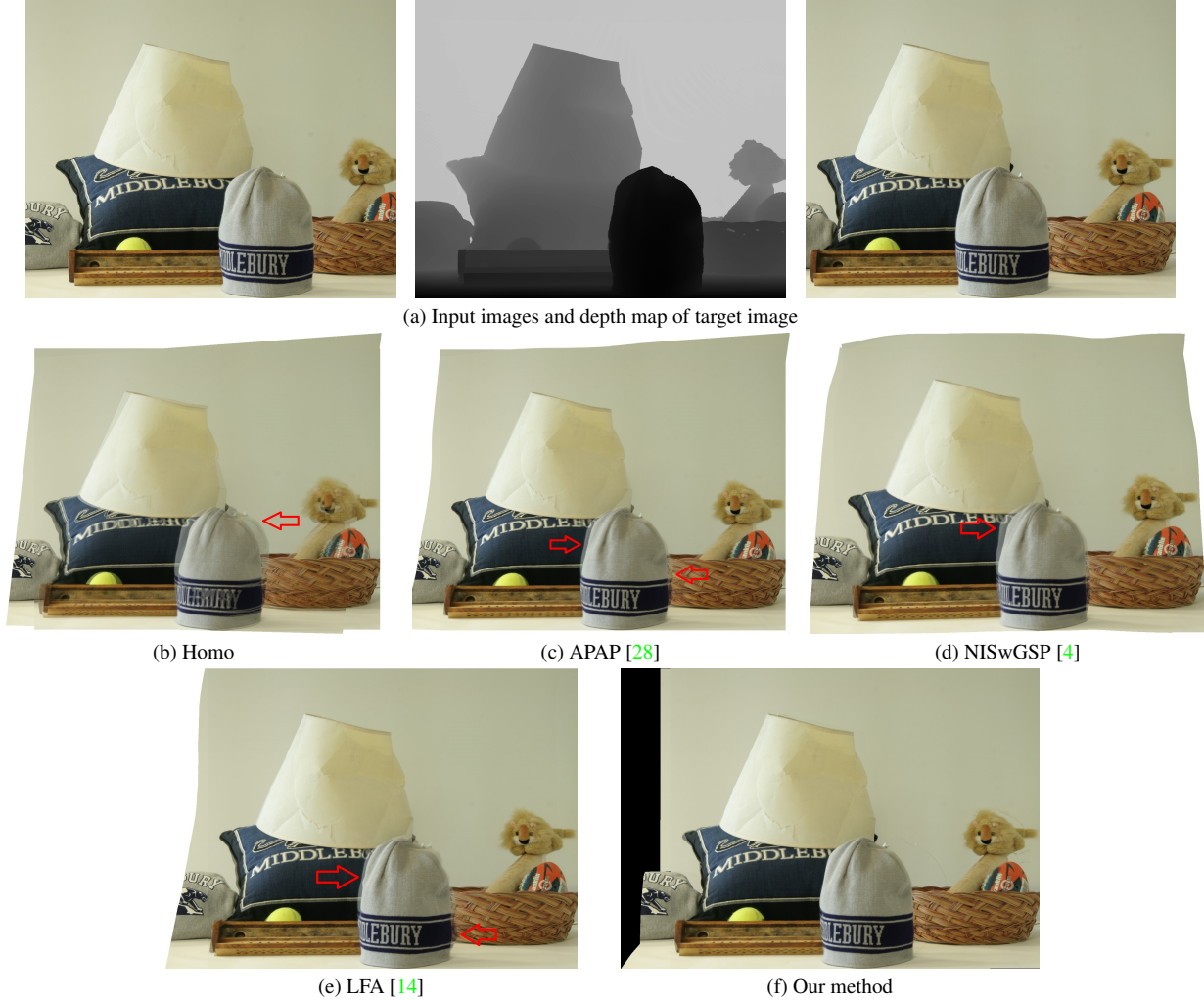


Figure 6. Comparisons with state-of-the-art NIS methods on the *Midd2* test case (best view in color and zoom in).

---

**Algorithm 3** Natural Image Stitching using Depth Maps.

---

**Require:**  $I_t$  and  $I_r$ ;

**Ensure:** Panorama  $I_m$ .

- 1: Extract a depth map of  $I_t$ ;
  - 2: Extract a set of point matches between  $I_t$  and  $I_r$ ;
  - 3: Extract a triangulation of  $I_t$ ;
  - 4: Estimate  $H_\infty$  and  $e'$  via Algorithm 1;
  - 5: Estimate  $\{H_\Delta\}$  via Algorithm 2;
  - 6: Warp  $I_t$  to  $I_w$  via backward texture mapping;
  - 7: Composite  $I_w$  and  $I_r$  via average blending to create  $I_m$ .
- 

## 5. Experiments

A series of comparison experiments are conducted to evaluate the performance of our proposed NIS method. The comparing methods include global homography (Homo), APAP [28], NISwGSP [4] and LFA [14]. The parameters

of existing methods are set as suggested by the original papers. In the experiment, we use VLFeat [26] to extract and match SIFT [21] feature points, use our robust fitting algorithm to remove outliers. To ensure a fair comparison, the same matching data are used in all tested methods except the NISwGSP method which is implemented in C++. To highlight the accuracy of image alignment, all stitching results are generated via simple average blending.

### 5.1. Results comparison

Fig. 6 demonstrates the comparison results of *Midd2* test case in Middlebury. Parallax can be seen from the relative position of the lampshade, the hat and the toy in the input images shown in Fig. 6(a). Obvious misalignments exist in the region of the hat in the results of Homo, APAP, NISwGSP and LFA, as shown in Fig. 6(b)-(e). Besides, the results of Homo, APAP and LFA also suffer from unnaturalness distortions on the left boundary. Our method generates

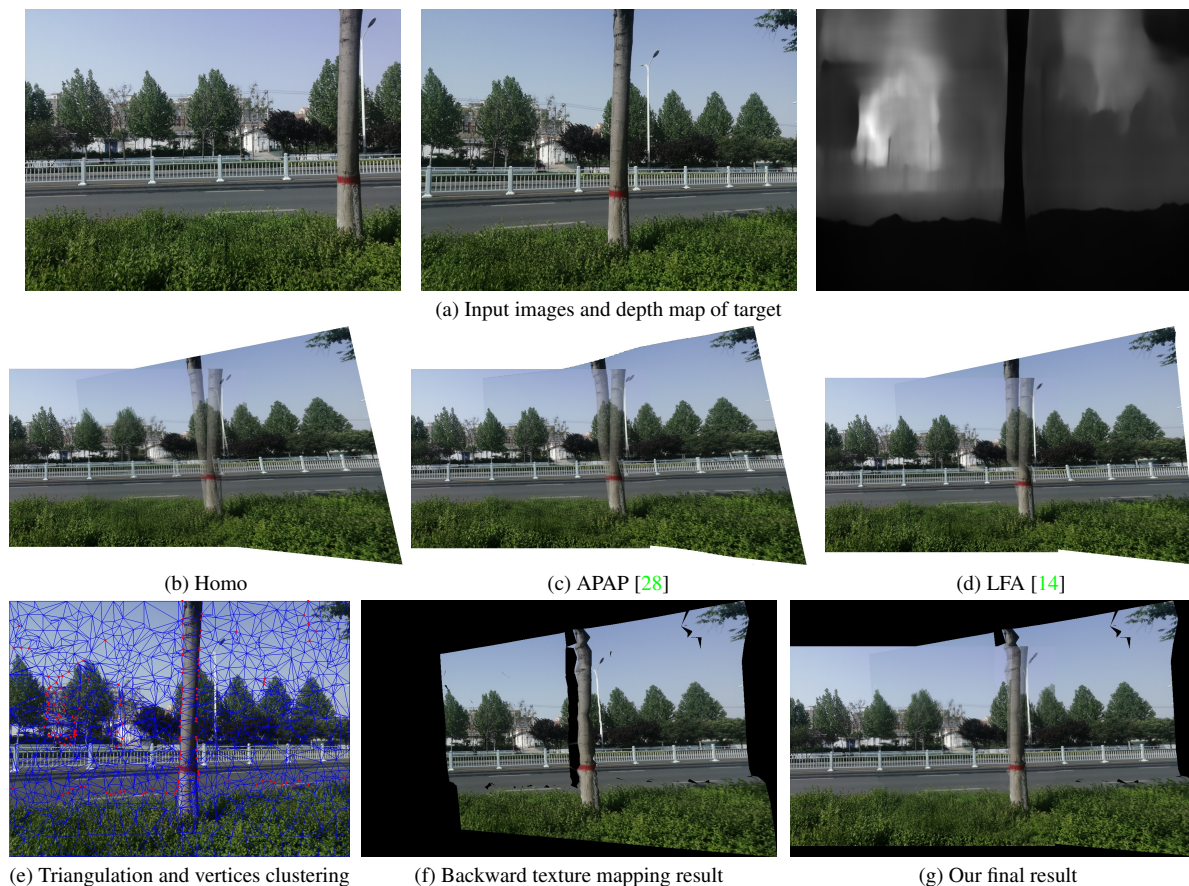


Figure 7. Failure example for wide-baseline test case. All the warping models fail to align the tree trunk.

a satisfactory result that is accurately aligned in the overlapping region and virtually natural in the non-overlapping region (see Fig. 6(f)).

Due to the limitation of pages, only one comparison result is presented. More comparison results on other datasets are provided in the supplementary material.

## 5.2. Limitation and failure examples

Our method assumes that the depth estimation for the target image is relatively accurate. Besides, the triangulation of the target image is assumed to be coplanar in the space for every triangular domain.

Fig. 7 shows a failure example of our proposed method. Input images in Fig. 7(a) are of large camera baseline and drastic depth variation. Obvious parallax can be observed from the relative position of the tree trunk and the background. Due to the estimated depth map of the target image is not accurate enough, the Delaunay triangulation and the subsequent depth values clustering are error-prone (see Fig. 7(e-f)). Note that with the help of depth data, our method still generates a more natural-looking stitching result in the non-overlapping region than other warping models (see Fig.

7(b-d)).

## 6. Conclusion

This paper proposed a NIS method using depth maps. Our main contribution is providing an adaptive method that leverages depth maps in NIS to address the challenge of parallax. Experimental results show that the proposed method not only provides accurate alignment in the overlapping regions, but also virtual naturalness in the non-overlapping region.

## References

- [1] Radhakrishna Achanta, Appu Shaji, Kevin Smith, Aurelien Lucchi, Pascal Fua, and Sabine Süsstrunk. Slic superpixels compared to state-of-the-art superpixel methods. *IEEE Trans. Pattern Anal. Mach. Intell.*, 34(11):2274–2282, 2012. 5
- [2] Che-Han Chang, Yuuki Sato, and Yung-Yu Chuang. Shape-preserving half-projective warps for image stitching. In *IEEE Conf. Comput. Vis. Pattern Recog.*, pages 3254–3261, 2014. 1, 3



- [3] Shenchang Eric Chen and Lance Williams. View interpolation for image synthesis. In *Proceedings of the 20th Annual Conference on Computer Graphics and Interactive Techniques*, SIGGRAPH '93, page 279–288, New York, NY, USA, 1993. Association for Computing Machinery. [3](#)
- [4] Yu-Sheng Chen and Yung-Yu Chuang. Natural image stitching with the global similarity prior. In *Eur. Conf. Comput. Vis.*, pages 186–201, 2016. [1](#), [2](#), [3](#), [7](#)
- [5] Martin A Fischler and Robert C Bolles. Random sample consensus: a paradigm for model fitting with applications to image analysis and automated cartography. *Communications of the ACM*, 24(6):381–395, 1981. [5](#)
- [6] Junhong Gao, Seon Joo Kim, and Michael S Brown. Constructing image panoramas using dual-homography warping. In *IEEE Conf. Comput. Vis. Pattern Recog.*, pages 49–56, 2011. [1](#), [2](#), [4](#)
- [7] Junhong Gao, Yu Li, Tat-Jun Chin, and Michael S Brown. Seam-driven image stitching. *Eurographics*, pages 45–48, 2013. [1](#)
- [8] Clement Godard, Oisin Mac Aodha, Michael Firman, and Gabriel J. Brostow. Digging into self-supervised monocular depth estimation. In *Int. Conf. Comput. Vis.*, October 2019. [1](#), [4](#)
- [9] R. I. Hartley and A. Zisserman. *Multiple View Geometry in Computer Vision*. Cambridge University Press, second edition, 2004. [1](#)
- [10] Hossam Isack and Yuri Boykov. Energy-based geometric multi-model fitting. *Int. J. Comput. Vis.*, 97(2):123–147, 2012. [5](#)
- [11] Qi Jia, ZhengJun Li, Xin Fan, Haotian Zhao, Shiyu Teng, Xinchen Ye, and Longin Jan Latecki. Leveraging line-point consistency to preserve structures for wide parallax image stitching. In *IEEE Conf. Comput. Vis. Pattern Recog.*, pages 12186–12195, June 2021. [3](#)
- [12] K. Joo, N. Kim, T. Oh, and I. S. Kweon. Line meets as-projective-as-possible image stitching with moving dlt. In *IEEE Int. Conf. Image Process.*, pages 1175–1179, 2015. [2](#)
- [13] Kyu-Yul Lee and Jae-Young Sim. Warping residual based image stitching for large parallax. In *IEEE Conf. Comput. Vis. Pattern Recog.*, June 2020. [1](#), [3](#)
- [14] Jing Li, Baosong Deng, Rongfu Tang, Zhengming Wang, and Ye Yan. Local-adaptive image alignment based on triangular facet approximation. *IEEE Trans. Image Process.*, 29:2356–2369, 2019. [1](#), [2](#), [3](#), [7](#), [8](#)
- [15] N. Li, Y. Xu, and C. Wang. Quasi-homography warps in image stitching. *IEEE Trans. Multimedia*, 20(6):1365–1375, 2018. [1](#), [3](#)
- [16] Shiwei Li, Lu Yuan, Jian Sun, and Long Quan. Dual-feature warping-based motion model estimation. In *Int. Conf. Comput. Vis.*, pages 4283–4291, 2015. [1](#)
- [17] T. Liao and N. Li. Single-perspective warps in natural image stitching. *IEEE Trans. Image Process.*, 29:724–735, 2020. [1](#), [3](#)
- [18] Chung-Ching Lin, Sharathchandra U Pankanti, Karthikeyan Natesan Ramamurthy, and Aleksandr Y Aravkin. Adaptive as-natural-as-possible image stitching. In *IEEE Conf. Comput. Vis. Pattern Recog.*, pages 1155–1163, 2015. [1](#), [3](#)
- [19] Kaimo Lin, Nianjuan Jiang, Loong-Fah Cheong, Minh Do, and Jiangbo Lu. Seagull: Seam-guided local alignment for parallax-tolerant image stitching. In *Eur. Conf. Comput. Vis.*, pages 370–385, 2016. [1](#)
- [20] Kaimo Lin, Nianjuan Jiang, Shuaicheng Liu, Loong-Fah Cheong, Minh Do, and Jiangbo Lu. Direct photometric alignment by mesh deformation. In *IEEE Conf. Comput. Vis. Pattern Recog.*, pages 2701–2709. IEEE, 2017. [1](#)
- [21] David G Lowe. Distinctive image features from scale-invariant keypoints. *Int. J. Comput. Vis.*, 60(2):91–110, 2004. [4](#), [7](#)
- [22] Eric Penner and Li Zhang. Soft 3d reconstruction for view synthesis. *ACM Trans. Graph.*, 36(6), Nov. 2017. [3](#)
- [23] Daniel Scharstein and Chris Pal. Learning conditional random fields for stereo. In *IEEE Conf. Comput. Vis. Pattern Recog.*, pages 1–8, 2007. [2](#)
- [24] Meng-Li Shih, Shih-Yang Su, Johannes Kopf, and Jia-Bin Huang. 3d photography using context-aware layered depth inpainting. In *IEEE Conf. Comput. Vis. Pattern Recog.*, pages 8025–8035, 2020. [3](#)
- [25] Richard Szeliski. Image alignment and stitching: A tutorial. *Foundations and Trends® in Computer Graphics and Vision*, 2(1):1–104, 2006. [1](#)
- [26] Andrea Vedaldi and Brian Fulkerson. Vlfeat: An open and portable library of computer vision algorithms. In *Proceedings of the 18th ACM International Conference on Multimedia*, pages 1469–1472, 2010. [7](#)
- [27] Olivia Wiles, Georgia Gkioxari, Richard Szeliski, and Justin Johnson. Synsin: End-to-end view synthesis from a single image. In *IEEE Conf. Comput. Vis. Pattern Recog.*, pages 7465–7475, 2020. [3](#)
- [28] Julio Zaragoza, Tat-Jun Chin, Quoc-Huy Tran, Michael S Brown, and David Suter. As-projective-as-possible image stitching with moving dlt. *IEEE Trans. Pattern Anal. Mach. Intell.*, 7(36):1285–1298, 2014. [1](#), [2](#), [5](#), [7](#), [8](#)
- [29] Fan Zhang and Feng Liu. Parallax-tolerant image stitching. In *IEEE Conf. Comput. Vis. Pattern Recog.*, pages 3262–3269, 2014. [1](#), [3](#)
- [30] Guofeng Zhang, Yi He, Weifeng Chen, Jiaya Jia, and Hujun Bao. Multi-viewpoint panorama construction with wide-baseline images. *IEEE Trans. Image Process.*, 25(7):3099–3111, 2016. [1](#), [3](#)
- [31] J. Zheng, Y. Wang, H. Wang, B. Li, and H. M. Hu. A novel projective-consistent plane based image stitching method. *IEEE Trans. Multimedia*, 21(10):2561–2575, 2019. [1](#), [2](#)
- [32] Tinghui Zhou, Richard Tucker, John Flynn, Graham Fyffe, and Noah Snavely. Stereo magnification: Learning view synthesis using multiplane images. *ACM Trans. Graph.*, 37(4), July 2018. [3](#)